Fuel 302 (2021) 121115

Contents lists available at ScienceDirect

Fuel

journal homepage: www.elsevier.com/locate/fuel

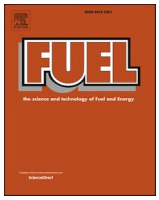

Full Length Article

Combustion performance in a cavity-based combustor under subatmospheric pressure

Zhixin Zhu [a,b], Yakun Huang [b,c,*], Huangwei Zhang [c], Xiaomin He [b,*]

[a] School of Aeronautics and Astronautics, Zhejiang University, Hangzhou 310027, China
[b] College of Energy and Power Engineering, Nanjing University of Aeronautics and Astronautics, Nanjing, Jiangsu 210016, China
[c] Department of Mechanical Engineering, National University of Singapore, Singapore 117576, Singapore

ARTICLE INFO

Keywords:
Cavity
Flameholder
Flame stability
Low pressure
Combustion efficiency

ABSTRACT

Combustion performance and flame stabilization mechanism of the flameholder under the subatmospheric pressure are the foundation for the design of high-altitude operating aircraft. An experimental cavity-based combustor was developed to explore the combustion performance in low pressure. Four low pressures of 0.03, 0.04, 0.05 and 0.06 MPa were validated to investigate the effect of inlet pressure on the flame stability limits, lean ignition and blowout process, combustion efficiency, and outlet temperature profiles. A unique lean spark ignition process was discovered at 0.03 MPa that the flame downstream of the V-type flameholder promotes the formation of the piloted flame in the cavity. Results indicate that the pressure reduction decreases the spray flame propagation, subsequently weakening flame stability and combustion efficiency. With the inlet pressure decreases, the pilot fuel injected into the cavity still maintains effective combustion, while the declining combustion is achieved in the mainstream fuel. This phenomenon suggests that increasing the pilot fuel proportion in the combustion chamber will enhance the combustion in ultra-low pressure.

1. Introduction

High-altitude in 11–44 km, one of the most promising and challenging spaces [1] urgently needs broadening the flame stability [2] and improving the combustion efficiency [3] under the condition of the subatmospheric pressure [4] and high-speed [5]. At present, the ramjet [6], scramjet [7], and various combined cycle engines, such as turbine-based combined cycle (TBCC) [8], rocket-based combined cycle (RBCC) [9], have been developed for flight missions in this space. Whatever the propulsion system, the reliable and efficient combustion chamber is essential for stable flight, where the flame cannot be stabilized without a cavity or other flameholder [10,11].

In the combustion chamber of all aerospace vehicles, the primary flame stabilization device includes the cavity-based flameholder [12] and bluff-body-based flameholder [13], such as V-type stabilizer, evaporating flameholder [14], and struts [15]. Generally, the spray flame of aerospace engines is stabilized in the recirculation zone [16], where the fresh fuel/air mixture is ignited by the hot burned gas [17]. The recirculation zone formed by the suction of the low-pressure area downstream of the V-type flameholder is easily destroyed by the change of the inlet velocity and fluid density [18]. Whereas the vortex "locked" in the cavity shows exceptional stability in a wide operating range [12]. The experimental results [19] revealed that the operating range of the trapped vortex cavity is 40% wider than that of the bluff-body-based flameholder in the gas turbine combustor. Besides, the lean blowout equivalence ratio and relight altitude in the cavity-based flameholder are ~50% lower and 33% higher than that in conventional combustors, respectively [20]. Therefore, the cavity-based flameholder is promising for the high-altitude engine [21], and its low-pressure combustion performance is also worth testing and verification.

Extensive studies have been experimentally and numerically conducted to investigate the flow field [22], fuel distribution [23], and combustion performance [24] of the cavity-based flameholder. An excellent combustion efficiency larger than 92% was achieved by the cavity-based flameholder at atmospheric pressure fueled with kerosene [25], and it was higher than 94% with methane fuel [26]. Besides, the fluid–structure of the dual-vortex trapped in the cavity was proved to be the main feature for excellent flame stabilization [27]. Meanwhile, different fuel injection modes were compared by evaluating the flame stability limits [28] and combustion efficiency [29]. The results

* Corresponding authors at: College of Energy and Power Engineering, Nanjing University of Aeronautics and Astronautics, Nanjing, Jiangsu 210016, China (Y. Huang & X. He).
E-mail addresses: yakunh@nuaa.edu.com (Y. Huang), hxm@nuaa.edu.com (X. He).

https://doi.org/10.1016/j.fuel.2021.121115
Received 20 February 2021; Received in revised form 2 May 2021; Accepted 12 May 2021

indicated the higher combustion efficiency and lower ignition fuel/air ratio were contributed by uniformly distributing [28] and preheating [30] fuel nozzles arranged in the fore-wall [29] of the cavity. The interaction between the mainstream flow and cavity flow [31], turbulence intensity [32], emissions characteristics [33], and combustion in scramjet engine [34] were also reported at different inlet Mach numbers and temperatures. However, the conditions of the combustor inlet directly affect the flame stability limits [35] and combustion efficiency [36]. As the flight altitude increases, low-pressure combustion will inevitably occur. The pressure reduction caused by rising altitude is a severe threat and drop to the combustion performance of the combustion chamber [37]. The limited publications on subatmospheric combustion present significant challenges and difficulties for designing the high-altitude propulsion system.

For subatmospheric combustion, the research topics are mainly divided into plateau fire prevention [38] and propulsion system [39]. The latter studies systematically show the damage of the pressure reduction to the spray combustion performance [40]. The experimental results [41] demonstrated that the combustion efficiencies were 28% and 39% with the inlet pressure of 0.034 MPa (flight altitude at 8.4 km). Read [42] found that the generated kernel cannot be stabilized, and it was disintegrated rapidly when the pressure less than 0.04 MPa. Furthermore, an increased ignition delay time was achieved by the decrease in pressure and temperature, and this phenomenon became significantly when the temperature lower than 700 K [43,44]. Obviously, reducing the pressure will weaken the chemical reaction rate, reduce the flame stability limit and combustion efficiency. The subatmospheric pressure poses a significant challenge to flame stability and combustion efficiency, which has not been adequately understood and addressed in publications. The solutions to subatmospheric combustion are still scarce but need urgent attention.

Based on the above, a cavity-based flameholder with a novel air-assisted multi-point injector has been designed to explore the feasibility of the high-altitude flight. Compared with previous studies, the design of this paper combines the superior stability of fluid–structure in the cavity and the effective flame propagation of the V-type flameholder in the mainstream. The flame stability limits and combustion efficiency are experimentally investigated under the conditions of pressure 0.03–0.06 MPa, Mach number 0.2, and temperature 700 K. The lean ignition and blowout processes in the cavity were first measured at ultra-low pressure by the high-speed camera, which attempts to provide an acceptable analysis for the combustion performance discrepancies resulted by the inlet pressure. The outlet temperature profiles assisted in constructing the subatmospheric flame distribution characteristics. The experimental results are expected to serve as a reference for the design of the high-altitude propulsion system. Additionally, the flame stabilization concept combined with the cavity and radial V-type flameholder, not limited to a V-type stabilizer and includes evaporating flameholder, provides valuable guidance for broadening the combustion boundary and improving the spray combustion efficiency.

2. Experimental description

2.1. Cavity-based flameholder design

A system flame stabilizing device comprises the pilot flameholder and the mainstream flameholder, as shown in Fig. 1. The pilot flameholder, stabilizing the combustion in whole operating conditions, is a trapped vortex cavity (TVC) device. The mainstream flameholder is a radial V-type flameholder installed under the cavity with a sweepback of 30°, which diffuses the flame from the cavity to the entire combustion chamber and stops working under some special conditions. Both flameholders have independent fuel supply systems: an air-assisted multi-point injector (AMI) is adopted in the pilot flameholder. The plain orifice injector is used as a mainstream injector depicted in Fig. 2 (c). Besides, the spark plug is installed at the bottom of the cavity, and a

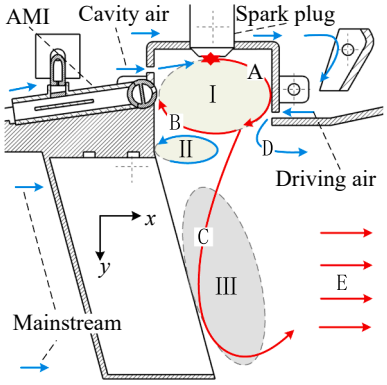

Fig. 1. Diagram of the cavity-based combustor.

diagram in a cross-section of the cavity-based flameholder combustor schematically illustrates the flow pattern and ignition process, as shown in Fig. 1.

Generally, the airflow distribution can be kept stable under different working conditions. The inflow is divided into two streams with a mass flow rate of 83% for mainstream and 17% for cavity and cooling. The cavity air is impacted by the driving air flows to the location *B* after flowing through the location *A* and forms a classical dual-vortex structure with low-pressure regions *I* and *II*. Then, a part of the cavity fluid flows to the mainstream at location *C* by the attractions of the low-pressure region *III* downstream of the V-type flameholder. Inevitably, some of the driving air also flows directly into the mainstream at location *D* and flows along with the fluid at location *C* to the location *E*. The liquid fuel is injected and mixed well with the air in the AMI. Sequentially, the fuel/air mixture flows into the cavity and will be ignited by the spark plug. Here, the mass flow rates of the cavity air, driving air, and AMI air account for 2.8%, 2.5%, and 0.57% of the total mass flow rate, respectively.

Fig. 2(a) shows a schematic of the rectangular test section with a size of 100 mm (width) × 136 mm (height). The flame morphology can be captured through the window. The spark plug (Model: TBH18N/70, Nanjing Tuoqi Technology Co.) is a surface discharge igniter plug with a diameter of 14 mm, which extends 2 mm from the bottom wall. The discharge of the spark plug is supported by a capacitive voltage generator unit (Model: TJG20-1, Nanjing Tuoqi Technology Co.), in which the single stored energy is 20 J, and its frequency is 8 Hz. The single duration is about 0.2 ms. Ten B-Type thermocouples (Model: WRR, PtRh30-Ptrh6, ϕ0.3) protected by the temperature rake is arranged 1000 mm downstream of the cavity center to measure the outlet temperature, as shown in Fig. 2(b). The reliable measurement range of the B-type thermocouple is 873–1973 K, and the uncertainty is 0.25%. In Fig. 2(b), ten temperature probes are divided into two rows (Pm and Ps) with a distance of 25 mm, among which the distance between the measuring points is also 25 mm, and the bottom measuring point is 15 mm from the wall surface. Fig. 2(c) and (d) shows the structure and dimensions of cavity-based flameholder. The AMI contains a plain orifice with a diameter of 0.5 mm and an evaporation tube, which has 21 holes with a diameter and interval of 1 mm and 4.4 mm, respectively. The detailed information can be found in [45]. The length of the cavity is 40 mm, and the heights of the fore-wall and after-wall are 35 mm and 26 mm, respectively. Besides, both cavity air and driving air are allowed to flow through the slot with a 2 mm width. Four pairs of orifice atomizers are distributed in the mainstream injector with an interval of 25 mm. Meanwhile, the liquid fuel sprays vertically to the mainstream from 0.5 mm orifices. Additionally, the mainstream injector is positioned parallel to the stabilizer at 150 mm upstream of it. The width of the radial V-type flameholder is 40 mm, and its contour is shown in the A-A section.

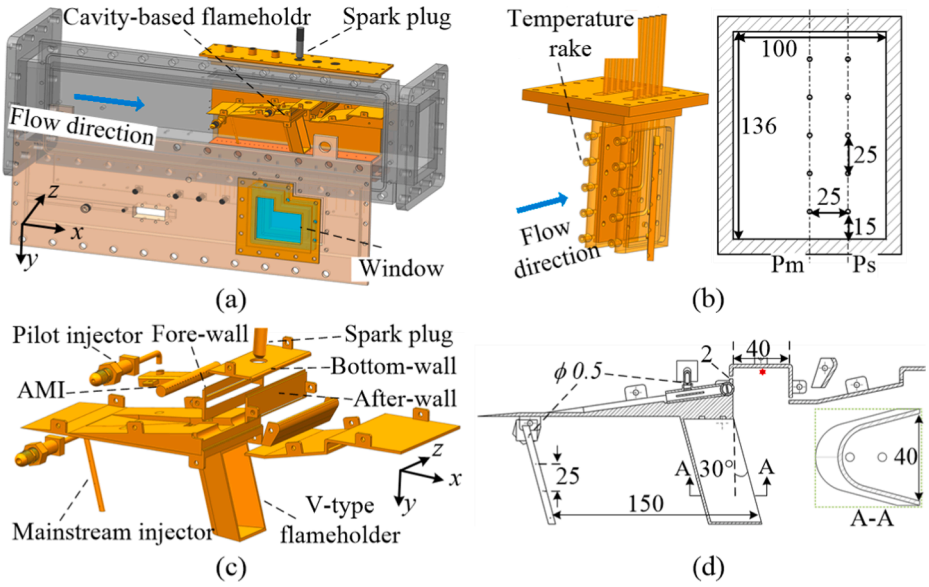

Fig. 2. Structure of (a) the cavity-based combustor, (b) temperature rake, (c) cavity-based flameholder, and (d) dimensions of flameholder. All dimensions in mm.

2.2. Experimental setup

Fig. 3 shows the experimental system, including the air supply system, inlet section, test section, measurement section, and exhaust system. The air supply system can provide the 1.5 kg/s dehumidified air as a maximum total mass flow rate measured by the orifice plate flowmeter with an uncertainty of 0.57%. The air can be heated by the electric heater to 500 K, and then the air temperature will unceasingly rise to 700 K by the pre-burner. Hence, the burned gas is mixed with the fresh air to maintain the oxygen mass fraction of 20.31%±0.49%. The total temperature and pressure are measured by a K-type thermocouple (Model: WRN, Ni Cr-Ni Si) and a pressure gauge (Model: YB-150, Hongqi Instrument Co.) at 350 mm and 220 mm upstream of the test section, respectively. Both uncertainties of the inlet temperature and pressure are 0.4%. Three vacuum pumps produce the subatmospheric pressure environment with a minimum pressure of 8 kPa in the exhaust system.

The high-speed camera (Model: Phantom v2012, Vision Resesarch, Inc.) is adopted to image the ignition and lean blowout process with a spatial resolution of 1,280 × 800. 10,000 fps is used for the sampling frequency with a time interval of 100 μs. Then, the exposure time is set to 50 μs.

In a subatmospheric pressure combustion test, the fuel flowmeter will show a slight lag due to the suction of the test channel, where the inhaled fuel cannot be accurately measured. Hence, the inlet pressure of the injector is used to evaluate the fuel mass flow rate. Fig. 4 shows the correlations between the fuel mass flow rate $\dot{m}_{fuel}$ and pressure drop ΔP_{fuel}, which are calibrated before and after the test. The pressure drop ΔP_{fuel} is the difference between the inlet of the injector and the test channel. Two correlations are fitted for the pilot and mainstream injector with the coefficient of determination R^2 not less than 0.97. Besides, RP-3 liquid fuel is used in this work, and the properties of the kerosene are listed in Table 1.

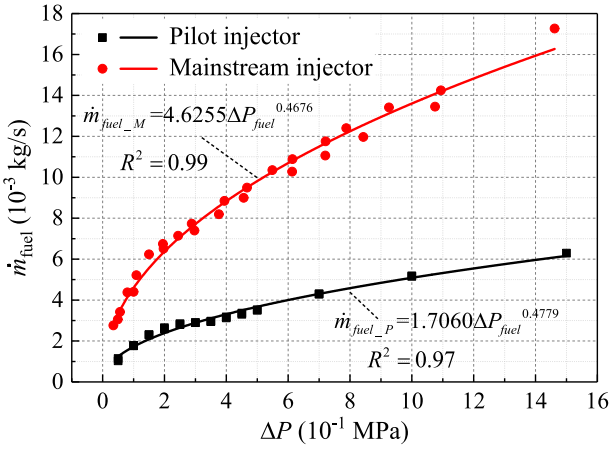

Fig. 4. Correlations between the fuel mass flow rate $\dot{m}_{fuel}$ and pressure drop ΔP_{fuel}.

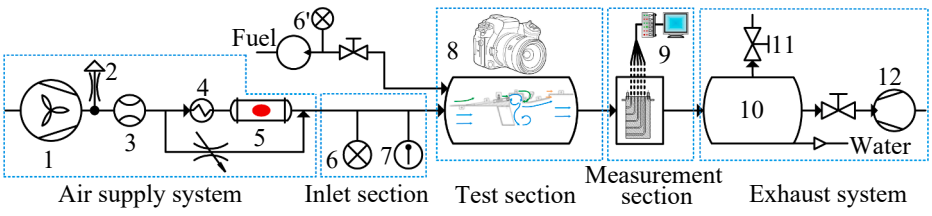

1 - Compressor	4 - Electrical heater	7 - Thermocouple	10 - Cooling tank
2 - Vent valve	5 - Pressure gage	8 - High-speed camera	11 - Valve
3 - Office meter	6 - K-Thermocouple	9 - NI system	12 - Vacuum pumb

Fig. 3 Schematic of the experimental system.

Fig. 3. Schematic of the experimental system.

Table 1
Properties of liquid kerosene [46,47].

Fuel	Molecular formulas	Density (kg/m^3)	Lower heating value (kJ/kg)	Viscosity ($\times 10^{-6}$ m^2/s)	Surface tension (N/m)	Boiling point (K)	Flashpoint (K)
RP-3	C12H23	780	≥42800	≥1.25	0.023	423–523	311

2.3. Experimental conditions

Four subatmospheric pressures of 0.03, 0.04, 0.05, and 0.06 MPa were designed to investigate the effect of the pressure on the combustion performance of cavity-based combustors. The inlet Mach number and temperature are 0.2 and 700 K, respectively. The range of the inlet Reynolds number is 1.157–3.443 × 10^5. The effect is embodied in the ignition, lean blowout, outlet temperature profile, and combustion efficiency. Here, the combustion efficiency is calculated by the enthalpy rise method [48], given as:

$$\eta = \frac{f_{in}(iT_{out} - iT_{in}) + C_{pout}T_{out} - C_{pin}T_{in} + f_{AB}(iT_{out} - iT_0)}{f_{AB}H_f} \quad (1)$$

where the iT_n represents the difference of enthalpy in isothermal combustion of T_n, the $C_{pn}T_n$ is the enthalpy of air with an average temperature of T_n, the f_{in} and f_{AB} are fuel/air ratio of the inlet of the combustor and fuel/air ratio of pre-burner respectively, the H_{f} is the low heating value and here is 43145 kJ/kg, subscripts *in* and *out* represent the inlet and outlet of the test tig, *0* represents the inlet of the pre-burner.

Errors in the experimental measurement are inevitable. Some uncertainties of directly measured quantities, such as inlet pressure and temperature, are determined by the measurement devices. These errors are evaluated by the T-distribution assumption with the confidence factor z = 1.96. Whereas some derived quantities, such as fuel flow rate and combustion efficiency, is estimated from [49]

$$\varepsilon = \sqrt{\varepsilon_1^2 + \varepsilon_2^2 + \cdots + \varepsilon_n^2} \quad (2)$$

where ε is the error limit, and ε_1, ε_2, ε_3, and ε_n are the error limits of the measured values. The detailed information can be found in Table 2.

Here, form Eq. (1), the error of combustion efficiency, as an example, can be calculated by

$$\varepsilon_\eta = \sqrt{\varepsilon_{f_{in}}^2 + \varepsilon_{f_{AB}}^2 + \varepsilon_{T_{in}}^2 + \varepsilon_{T_{out}}^2 + \varepsilon_{T_0}^2} \quad (3)$$

where the ε_η, ε_{fin}, ε_{fAB}, ε_{Tin}, ε_{Tout}, and ε_{T0} are the uncertainties of the combustion efficiency, test rig fuel/air ratio, pre-burner fuel/air ratio, inlet temperature, and outlet temperature.

The error of the fuel/air ratio ε_f is related to air mass flow rate and fuel mass flow rate, expressed as:

$$\varepsilon_f = \sqrt{\varepsilon_{\dot{m}_{air}}^2 + \varepsilon_{\dot{m}_{fuel}}^2} \quad (4)$$

Table 2
Experimental condition and error.

Variable	Method	Value	Error (%)
Inlet temperature, T_i (K)	K-type thermocouple	700	0.40
Inlet pressure, P_i (MPa)	Pressure gauge	0.03–0.6	0.40
Air massflow rate, $\dot{m}_{\mathrm{a}}$ (kg/s)	Orifice plate flowmeter	0.215–0.431	0.57
Inlet Mach number, *Ma*	$Ma = \dot{m}_{\mathrm{a}}/A(\lambda RT)^{1/2}$	0.2	0.57
Inlet Reynolds number, *Re* (10^5)	$Re = (P/RT)(\dot{m}_{\mathrm{a}}/A)\, d/\mu$	1.157–3.443	0.80
Fuel mass flow rate, $\dot{m}_{\mathrm{f}}$ 10^{-3}kg/s	$\dot{m}_{\mathrm{f}} = \alpha\Delta P_{fuel}^{\beta}$	0.49–26.36	0.40
Equivalence ratio, (φ_{total})	$\varphi_{\mathrm{total}} = \dot{m}_{\mathrm{f}}/(\dot{m}_{\mathrm{a}}q_{\mathrm{st}})$	0.034–0.910	0.70
Outlet temperature profile, T_o/T_{oavg}	B-type thermocouple	0.839–1.328	0.35
Combustion efficiency, η (%)	Enthalpy rise method	41.66–72.71	1.17

where the $\varepsilon_{\dot{m}air}$ and $\varepsilon_{\dot{m}fuel}$ are the errors of air mass flow rate and fuel mass flow rate.

The air mass flow rate $\dot{m}_{\mathrm{air}}$ is measured by the orifice plate flowmeter, which is calculated by:

$$\dot{m}_{air} = 1.4089\sqrt{\frac{(P_{air0} + \Delta P_{air})H}{T}} \quad (5)$$

where $\dot{m}_{\mathrm{air}}$ is the air mass flow rate; P_{air0} is the ambient pressure; P_{air} is the pressure upstream of the orifice plate flowmeter, both P_{air0} and P_{air} are measured by pressure gauges; H is the pressure difference between upstream and downstream of the orifice plate flowmeter, measured by U-type manometer with the uncertainty of 0.01%; T is the air temperature at orifice plate flowmeter, measured by K-type thermocouple.

Then, from Eq. (5), the $\varepsilon_{\dot{m}air}$ can be expressed as:

$$\varepsilon_{\dot{m}_{air}} = \sqrt{\varepsilon_H^2 + \varepsilon_T^2 + \varepsilon_P^2} = 0.57\backslash\% \quad (6)$$

Also, according to Fig. 4, the $\varepsilon_{\dot{m}fuel}$ can be expressed as:

$$\varepsilon_{\dot{m}_{fuel}} = \sqrt{\varepsilon_{m_{fuel}}^2 + \varepsilon_{\Delta P}^2} = 0.40\% \quad (7)$$

Hence, the $\varepsilon_f = 0.70\%$, which is calculated by the Eq. (4), Eq. (6), and Eq. (7). Also, the $\varepsilon_{Tin} = \varepsilon_{T0} = 0.40\%$ and $\varepsilon_{T0} = 0.25\%$ lead a result of $\varepsilon_\eta = 1.17\%$ from the Eq. (3).

3. Results and discussion

A successful combustion chamber, applied to the ramjet, is required to burn stably over a wide range of operating conditions with a high combustion efficiency. Meanwhile, flame propagation and disappearance can reproduce the design concept and scheme defects, and subsequent designs can be inspired. In this work, the flame stability limits, combustion efficiency, ignition, and lean blowout processes in normal and ultra-low pressure are experimentally investigated to explore the effect of inlet pressure on cavity-based combustor performance. Four subatmospheric pressures are conducted at the inlet Mach number of 0.2 and temperature of 700 K. All the tests are conducting in a stable condition, and the inlet conditions will only be adjusted after the working condition is completed. The flame stability limits are first discussed with different inlet pressure at $Ma = 0.2$ and $T_i = 700$ K.

3.1. Flame stability limits

The flame stability limits play an important role in the aircraft engine system. With the development of military applications, the operating conditions of ramjets continue to explore the high altitude, coupled with the low-pressure and low temperature. Thus the lean ignition and blowout limits are focused under the condition of subatmospheric pressure at $Ma = 0.2$ and $T_i = 700$ K, as shown in Fig. 5. As shown, the decreasing tendency of the equivalence ratios of lean ignition and blowout is achieved by the increase in inlet pressure. For lean ignition limit, the maximum ignition equivalence ratio obtained at $P_i = 0.03$ MPa is 0.116, which is 52.92% larger than that at $P_i = 0.06$ MPa. As mentioned in the introduction, the reduced chemical reaction rate, contributed by the decrease in pressure, increases the difficulty of lean ignition. At the same time, the density decreases with the reduction of pressure. Thus the weakened disruptive aerodynamic force ($\rho_{\mathrm{air}}u_{\mathrm{air}}^2$) reduces the atomization of the fuel droplet. Consequently, the ignition equivalence ratio increases as the inlet pressure decrease. Meanwhile, the lean blowout equivalence ratio varies from 0.034 to 0.058, with the

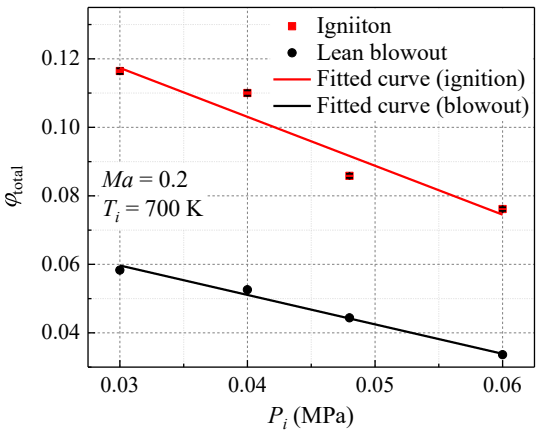

Fig. 5. Ignition and blowout limits with different inlet pressure at $Ma = 0.2$ and $T_i = 700$ K.

inlet pressure changes from 0.06 MPa to 0.03 MPa. The cavity-based flameholder exhibits excellent flame stability even in the low-pressure and high-speed environment. The fuel supply device AMI is adopted with the evaporation tube enhances the lean blowout limit. Hence, the average equivalence ratio of a lean blowout is 0.047, which is 51.37% less than that of lean ignition. Both the decreased trends of lean ignition and blowout equivalence ratios are linear, in which slopes of the fitted curves are −1.43 and −0.86, respectively. This is evidence that the reduction in pressure is more damaging to the lean ignition limit than that to the lean blowout. The detailed analysis will be discussed in conjunction with the lean ignition and blowout process.

3.2. Ignition and lean blowout process

In the ignition and lean blowout process test, only the pilot fuel injector is working. The minimum fuel mass flow rate, which can be ignited, has been provided by AMI before the spark plug discharging. Additionally, the lean blowout is achieved by reducing the fuel mass flow rate slowly during the combustion. The lean blowout process is very rapid and far less than the change of fuel mass flow rate, so it can be considered that the fuel equivalent ratio is fixed at the moment of the extinction.

The flame evolution during the ignition process is shown in Fig. 6. In this case, the inlet pressure is 0.06 MPa, the Mach number is 0.2, the temperature is 700 K, and the total equivalence is 0.076. As shown, the ignition process of cavity-based flameholder can be divided into four parts: the spark & kernel generation (*Phase* 1), flame growth in the cavity (*Phase* 2), flame growth in the V-type flameholder (*Phase* 3), and stable combustion (*Phase* 4). This process is highly consistent with the design concept of the cavity-based flameholder, as shown in Fig. 1. As excepted, the fuel droplet mixes well with the air in the evaporation tube, then the fuel/air mixture flows through the cavity and V-type flameholder successively. In *Phase* 1, the spark plug discharges at $t = 0$, which generates an ionization region with high temperature. Then the kernel appears and finally becomes stable at $t = 0.4$ ms. During the period of $t = 0.6$ ms to $t = 3.0$ ms, the flame kernel gradually grows to fill the low-pressure regions *I* and *II* in the cavity along with the flow at location A shown in Fig. 1. This signifies that the flame can be stabilized in the cavity and will propagate to the mainstream later. If the flame cannot fill the whole cavity space, that means the energy transported by the reflux air in location *B* is insufficient to ignite the fresh fuel/air mixture, and the extinction may consequently happen. After that, in *Phase* 3, the flame naturally propagates from the cavity to the low-pressure region *III* along with the fluid at location *C*. Finally, the flame

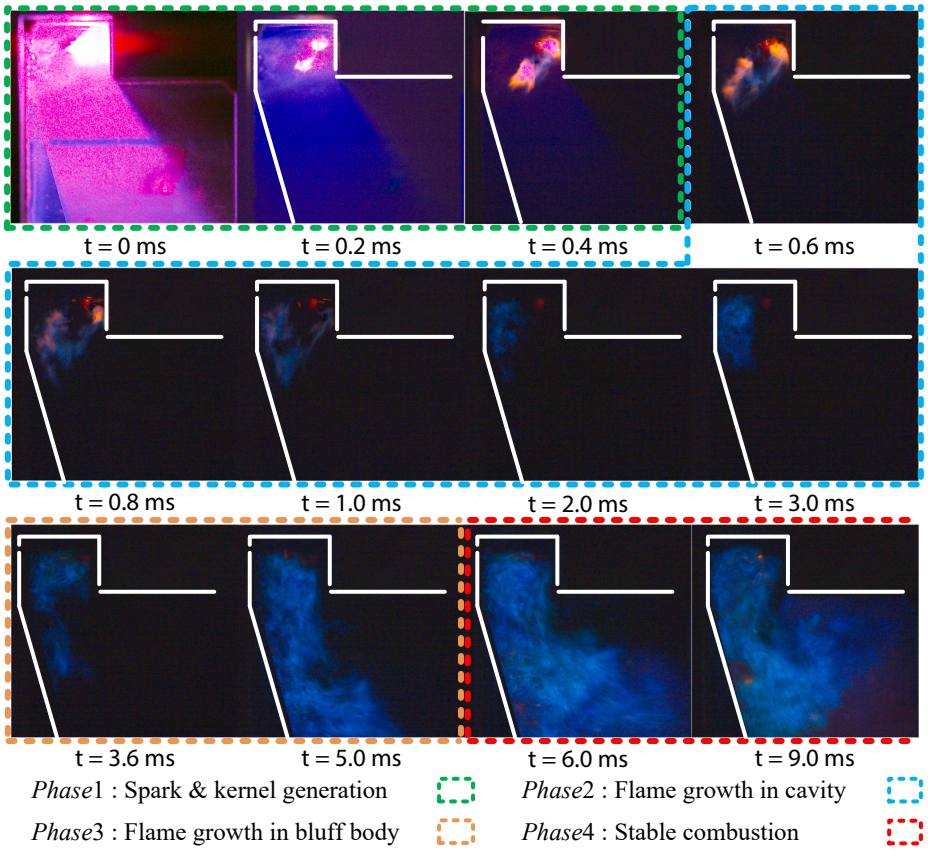

Fig. 6. Flame evolution of ignition under $P_i = 0.06$ MPa, $Ma = 0.2$, $T_i = 700$ K and $\varphi_{total} = 0.076$.

spreads to the whole combustion chamber and keeps stable combustion in *Phase* 4, reflecting a successful ignition.

Fig. 7 shows the flame evolution of ignition process under the condition of $P_i = 0.03$ MPa, $Ma = 0.2$, $T_i = 700$ K and $\varphi_{total} = 0.116$. Overall, the flame propagation in $P_i = 0.03$ MPa is more slowly than that in $P_i = 0.06$ MPa. Besides, the ignition delay time is 71.0 ms in $P_i = 0.03$ MPa, which is 11.8 times larger than that in $P_i = 0.06$ MPa. This indicates that the reduction of pressure has seriously affected the transmission and expansion of the flame, reflecting that the lean ignition equivalence ratio increases with the inlet pressure decreasing, as shown in Fig. 5. Moreover, the most unexpected change is that the flame kernel, generated in the cavity, will be stabilized in the recirculation zone downstream of the V-type flameholder (region *III*) and then spread to the cavity renewedly. It is the first discovery that *Phase* 2 and *Phase* 3 in $P_i = 0.03$ MPa is completely opposite to the ignition process in $P_i = 0.06$ MPa, and the interval of the flame spreads from the V-type flameholder to the cavity is much longer with the decrease in pressure. It directly indicates that the reduction in pressure weakens the reaction rate, so that the energy in reflux in location *B*, produced by the flame kernel, cannot ignite the fresh mixture, schematically shown in Fig. 1. After a steady accumulation of energy, the flame was finally ignited when the fuel/air mixture flows to the recirculation zone (region *III*) downstream of the V-type flameholder. Similarly, the fuel droplet in the cavity, especially in the evaporation tube, is promoted by the flame in region *III*. Then, the further evaporating of fuel and a higher temperature is achieved to facilitate combustion again, and the combustion chamber is ignited. It is worth noting that compared with the inlet condition of 0.06 MPa, the lowest equivalence ratio, igniting successfully, has increased by 52.63% in the $P_i = 0.06$ MPa. Meanwhile, 60 ms are consumed in *Phase* 3, which means that the pressure reduction weakens the chemical reaction rate and destroys the evaporation effect of the droplet.

Flame stability is reflected not only in the ignition process but also in the extinction characteristics. The lean blowout process is captured when the flame vanishes, which is achieved by continuously reducing the injector's pressure drop. As noted above, the pressure drop of a lean blowout is approximately considered constant in the interval between the flame vanishes. The process of the flame gradually contracting and decreasing is shown in Fig. 8. In this case, the inlet pressure is 0.03 MPa, the Mach number is 0.2, the temperature is 700 K, and the equivalence ratio is 0.058. Similarly, the lean blowout process is also divided into four stages: stable combustion, flame attenuation, the flame disappeared in the cavity, and extinction. As expected, the lean blowout process is the exact opposite of the ignition process at $P_i = 0.06$ MPa. In the flame extinction, the stable flame firstly attenuates from the recirculation zone (region *III*) downstream of the V-type flameholder. Then the flame collapses from the region *III* to the regions *I* and *II* in the cavity. Finally, the flame disappears gradually in the cavity, and the extinction happens. Combining Fig. 7 and Fig. 8 shows that the spray flame propagation and diffusion are highly correlated with fuel atomization, especially in ultra-low pressure at 0.03 MPa. The reduction of the pressure reduces the air density and weakens the disruptive aerodynamic force. Consequently, the secondary atomization of fuel droplets becomes worse. This phenomenon is particularly prominent in the combustor adopted with the evaporation tube. When the flame is stabilized in the cavity, the temperature rises with the evaporation tube heated. Then, the evaporation of the fuel droplets is intensified, which makes the fuel/air mixture to be ignited quickly in the cavity. Hence, the lean blowout process is utterly different from the ignition process at $P_i = 0.03$ MPa, and excellent flame stability is proved for the cavity-based flameholder at ultra-low pressure. Moreover, it also confirmed that the reducing trend of the lean blowout equivalence ratio is smaller than that of lean ignition shown in Fig. 5.

3.3. Combustion efficiency

Generally, the applicable combustor requires a wide range of flame

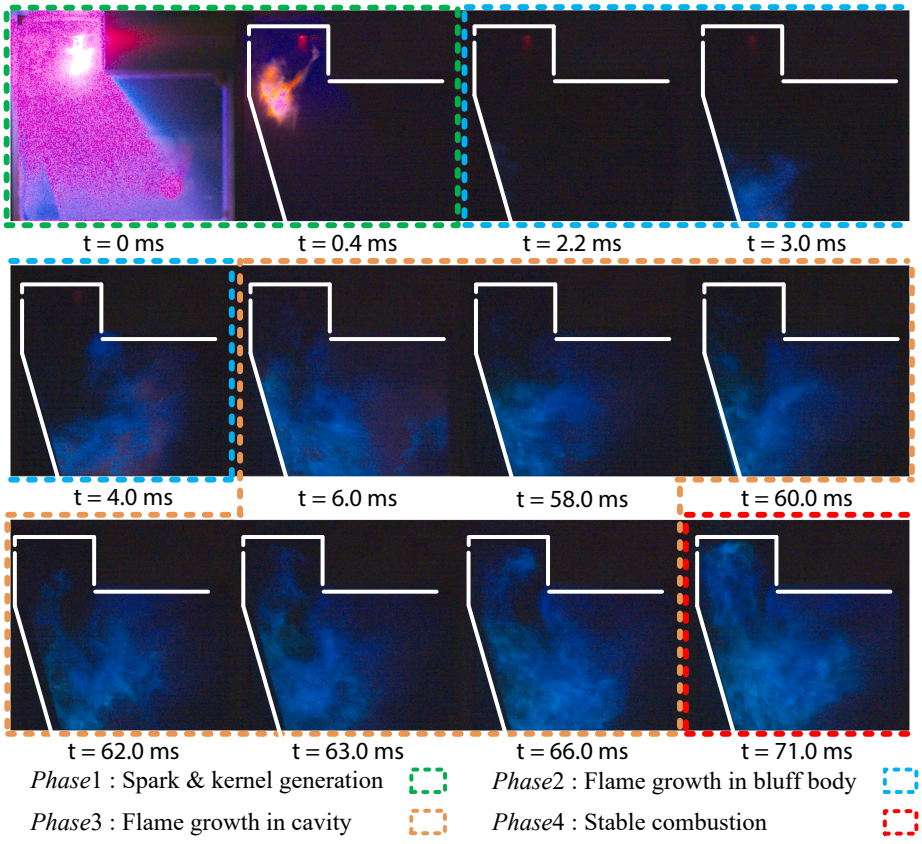

Fig. 7. Flame evolution of ignition under $P_i = 0.03$ MPa, $Ma = 0.2$, $T_i = 700$ K and $\varphi_{total} = 0.116$.

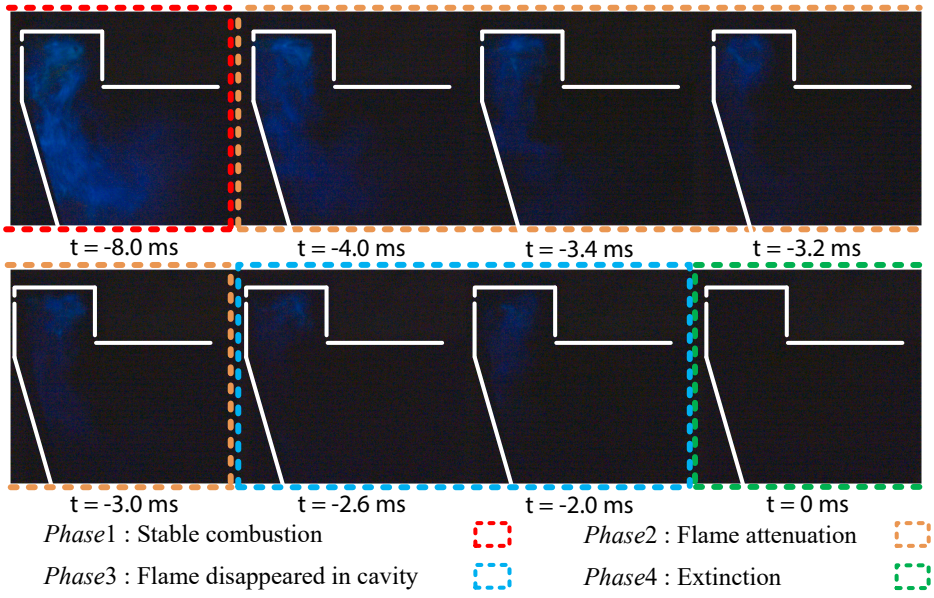

Fig. 8. Flame evolution of lean blowout under P_i = 0.03 MPa, Ma = 0.2, T_i = 700 K and φ_{total} = 0.058.

stability limits and no combustion efficiency less than 90%. However, at high altitudes, the combustion efficiencies are low for traditional burners and undiscovered for cavity-based flameholder. Here, the combustion efficiency tests are conducted at four subatmospheric pressure with different equivalence ratios. The combustion efficiency is evaluated by the enthalpimetric method with Eq. (1).

Fig. 9 shows the combustion efficiency curves with the equivalence ratio range of 0.297 to 0.910 when the inlet pressure varies from 0.03 MPa to 0.06 MPa. The inlet velocity and temperature are maintained at Mach 0.2 and 700 K. Overall, the combustion efficiency reduces with the inlet pressure decreasing from 0.06 MPa to 003 MPa. The highest combustion efficiency of ~ 100% is achieved at P_i = 0.06 MPa and φ_{total} = 0.296 or 0.301. Besides, the average combustion efficiency is 59.41% at P_i = 0.03 MPa, which is 6.03%, 13.83%, and 38.18% smaller than that in P_i = 0.04, 0.05, and 0.06 MPa, respectively. However, an unusual phenomenon has been discovered that the most combustion efficiencies in P_i = 0.04 MPa are larger than that in P_i = 0.05 MPa with the equivalence ratio range of 0.395 to 0.780 with the inlet pressure decreasing from 0.06 MPa to 0.03 MPa. Meanwhile, the combustion efficiency at the inlet pressure of 0.03 MPa shows unexpected stability, and its value is higher at the equivalence ratio larger than 0.70. It should be noted that the combustion efficiency does not decrease monotonically as the equivalence ratio increases. Instead, the peak of combustion efficiency curves happens between the equivalence ratio of about 0.45 and 0.63, then declines rapidly. Of course, a clear understanding of the combustion results requires information about the fuel supply and flame distribution. The fuel supply distribution is presented by the ratio of the fuel mass flow rate of the pilot to the total shown in Fig. 10, while the flame distribution is reflected by the flame image and outlet temperature profiles shown in Fig. 11.

Fig. 10 shows the pilot fuel proportion, which is evaluated by the ratio of fuel mass flow rate of the pilot to the total, expressed as $\varphi_{pilot}/\varphi_{total}$. Here, the fuel/air ratio and equivalence ratio are expressed as $q_{LBO} = m_{fuel}/m_{ac}$ and $\varphi = q_{LBO}/q_{st}$, where the q_{LBO} is the fuel/air ratio, m_{fuel} is the fuel flow rate for AMI, m_{ac} is the total airflow rate in a cavity, φ is the equivalence ratio, and q_{st} is the stoichiometric fuel/air ratio, which is 0.0672 for the RP-3 liquid fuel. As mention in section 3.1, the flame stability limit decreases with the reduction of inlet pressure, and the flame is mainly stabilized by the cavity. The fuel mass flow rate in the cavity needs to be enlarged to hold a stable flame. Therefore, the $\varphi_{pilot}/\varphi_{total}$ increases gradually with the decrease of the inlet pressure. Again, the decreased inlet pressure weakens the flame propagation and diffusion has been proved in section 3.2, which indicates that the efficient combustion is achieved in the recirculation zone represented as regions *I*, *II*and *III*, as shown in Fig. 1. Meanwhile, the highest

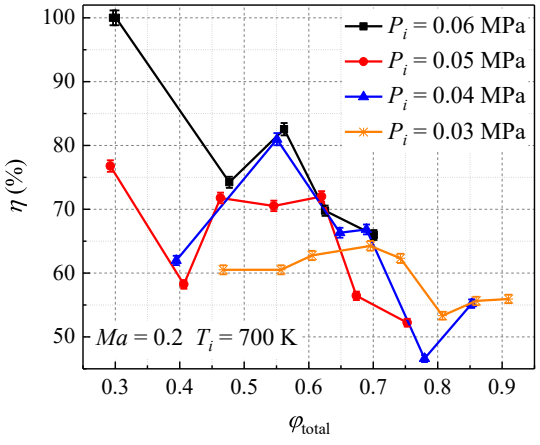

Fig. 9. Effect of inlet pressure on Combustion efficiency with the variation of equivalence ratio at Ma = 0.2 and T_i = 700 K.

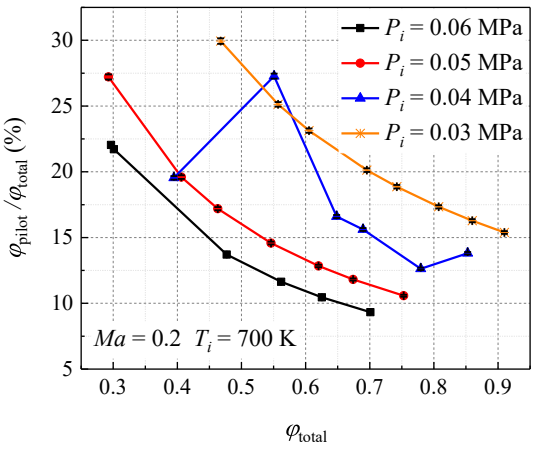

Fig. 10. Fuel supply proportion of the pilot fuel.

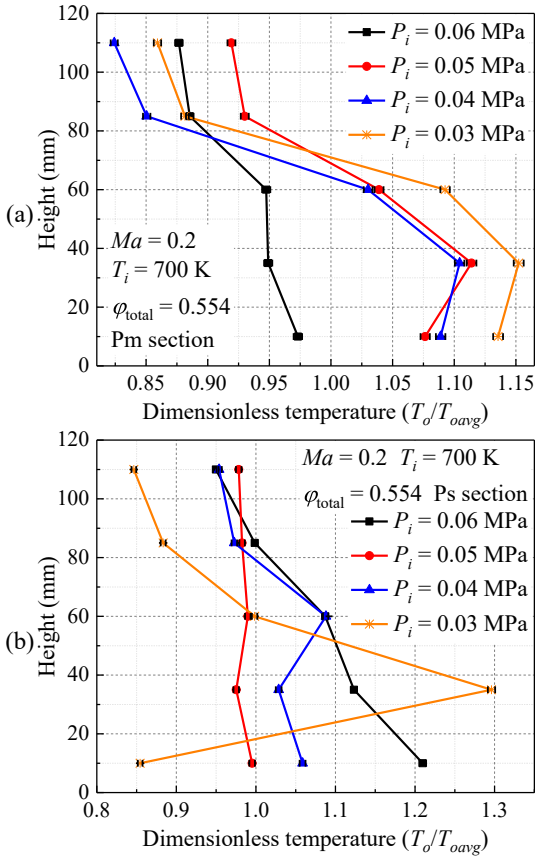

Fig. 11. Radial outlet temperature profiles with different inlet pressure at *Ma* = 0.2, T_i = 700 K, and φ_{total} = 0.554.

combustion efficiency points at P_i = 0.05 and 0.06 MPa also have a high $\varphi_{pilot}/\varphi_{total}$, which reflects that the higher pilot equivalence ratio contributes to higher combustion efficiency. Besides, the combustion efficiency increases from 61.98% to 80.97 with the $\varphi_{pilot}/\varphi_{total}$ increasing from 19.54% to 27.27% at P_i = 0.04 MPa, proving the positive correlation between the $\varphi_{pilot}/\varphi_{total}$ and combustion efficiency again. Building upon this knowledge base, the combustion efficiency at P_i = 0.04 MPa is higher than that at P_i = 0.05 MPa can be understood, and the combustion efficiency curve of the inlet pressure 0.03 MPa can also be explained well.

3.4. Outlet temperature profiles

Fig. 11 shows the radial outlet temperature profiles with different inlet pressures. Two rows (Pm and Ps) of the temperature probes (Pm and Ps) shown in Fig. 2 are adopted to measure the outlet pressure at *Ma* = 0.2, T_i = 700 K, and φ_{total} = 0.554. The outlet temperature is dimensionless by the averaged outlet temperature. According to the design concept demonstrated in Fig. 1, the fuel in the center section of the combustion chamber is mainly composed of the pilot fuel and little mainstream fuel involved in the recirculation zone downstream of the V-type flameholder (region *III*). This shows that the combustion effect of the central section may be better than that of the side sections. Furthermore, the combustion efficiency of pilot fuel and mainstream fuel are evaluated by the outlet temperature in Pm and Ps sections, respectively.

As shown in Fig. 11(a), the radial outlet temperature profiles in the Pm section distribute as the hook form at the pressure of 0.05, 0.04, and 0.03 MPa. The highest temperature occurs at 35 mm, which indicates that the fuel droplets injected from AMI flow into the recirculation zone downstream of the V-type flameholder (region *III*), as shown in Fig. 1, and participate in the violent combustion reaction occurring the downstream of the region *III*. The radial outlet temperature shows a high non-uniform at P_i = 0.03 MPa with the highest T_o/T_{avg} of 1.14, which is 24.34% higher than that at the height of 115 mm. This means that the flame distribution is uneven at P_i = 0.03 MPa, as well as the conditions of P_i = 0.04 and 0.05 MPa. However, a flat radial outlet temperature profile is obtained at P_i = 0.06 MPa, reflecting a uniform flame distribution. Thus, it can be seen from the radial outlet temperature profiles that the flame in the center section (Ps) becomes more uneven as the inlet pressure decreases from 0.06 MPa to 0.03 MPa. This again demonstrates that the reduction of inlet pressure will weaken the flame propagation, thereby reducing the combustion efficiency.

The radial outlet temperature profiles are plotted in Fig. 11(b). As shown, the radial outlet temperature curves of P_i = 0.04, 0.05, and 0.06 MPa are relatively gentle. Four outlet temperature values in the P_i = 0.06 MPa are larger than 1.0, which indicates that most mainstream fuel droplets participated in the combustion reaction and the flame distribution is relatively uniform. Then, all outlet temperature values smaller than the average outlet temperature at P_i = 0.05 MPa, reflecting a poor combustion state. The unexpected is that the radial outlet temperature profile in the Ps section at P_i = 0.04 MPa is higher than that at P_i = 0.05 MPa. As an accident of combustion efficiency, this is mainly due to the large proportion of $\varphi_{pilot}/\varphi_{total}$ under the condition of P_i = 0.04 MPa and φ_{total} = 0.554, as shown in Fig. 10. Besides, when the equivalence ratio maintains at 0.554, the combustion efficiency at P_i = 0.04 MPa is larger than that at P_i = 0.05 MPa and smaller than that at P_i = 0.06 MPa. This phenomenon indicates that the effective combustion reaction is mainly conducted in the recirculation zone, such as region *I* in the cavity and region *III* downstream of the V-type flameholder shown in Fig. 1. The lowest combustion efficiency is obtained at P_i = 0.03 MPa. The uneven outlet temperature distribution appears again in the Ps section, which fully demonstrates that combustion is not sufficient at ultra-low pressure even with a large proportion $\varphi_{pilot}/\varphi_{total}$. However, when the equivalence ratio is bigger enough, here the value is about 0.7, the combustion efficiency decreases promptly with the reduction of $\varphi_{pilot}/\varphi_{total}$. Then the combustion efficiency at P_i = 0.03 MPa is highest in the range of the equivalence ratio larger than 0.7, as shown in Fig. 9.

4. Concluding remarks

In widespread attention of high-altitude flight with the subatmospheric combustion program, the flame stability and combustion efficiency variation affected by the inlet pressure was discussed in this work. Four inlet pressures, including 0.03, 0.04, 0.05, and 0.06 MPa, were designed to explore the combustion performance of a novel cavity-based flameholder with the inlet Mach number of 0.2 and temperature of 700 K. Experimental results show that the reduction of the inlet pressure has a significant influence on flame propagation and combustion performance. The results have a considerable reference value for ramjet design.

The reduction of inlet pressure weakens the flame propagation and consequently decreases the combustion performance. Low pressure, such as inlet pressure of 0.03 MPa, changes the process of spray flame evolution, especially mutual promotion between the cavity flame and mainstream flame downstream of the radial V-type flameholder. When the inlet pressure is 0.03 MPa, the flame kernel, generated in the cavity, would be stabilized in the recirculation zone downstream of the V-type flameholder and then spread to the cavity renewedly. This ignition flame process is entirely different from that at 0.06 MPa or higher pressures. The reduction of flame stability and combustion efficiency contributed by decreased inlet pressure has been proved in cavity-based flameholder. It worth noting that the combustion of mainstream fuel is not complete, but the pilot fuel supplied in the cavity has effective combustion. Current experimental data suggest that the pilot fuel proportion in the combustion chamber should be increased to maintain efficient combustion under ultra-low pressure conditions.

Future work contains a more detailed lean ignition and blowout process, the interaction between the pilot fuel and mainstream fuel, and the flame characteristics under broad operating conditions.

CRediT authorship contribution statement

Zhixin Zhu: Conceptualization, Methodology, Investigation, Software, Visualization, Data curation, Validation, Writing - original draft. **Yakun Huang:** Conceptualization, Methodology, Investigation, Data curation, Validation, Writing - review & editing. **Huangwei Zhang:** Investigation, Writing - review & editing, Visualization, Supervision. **Xiaomin He:** Conceptualization, Writing - review & editing, Supervision.

Declaration of Competing Interest

The authors declare that they have no known competing financial interests or personal relationships that could have appeared to influence the work reported in this paper.

Acknowledgment

This work was supported by the National Science and Technology Major Project (No. 2017-Ill-0008-0034). YH gratefully acknowledges the financial support from the China Scholarship Council (No. 201906830096).

References

[1] Li Z, Moradi R, Marashi SM, Babazadeh H, Choubey G. Influence of backward-facing step on the mixing efficiency of multi microjets at supersonic flow. Acta Astronaut 2020;175:37–44. https://doi.org/10.1016/j.actaastro.2020.05.003.
[2] Cai Z, Zhu J, Sun M, Wang Z, Bai XS. Laser-induced plasma ignition in a cavity-based scramjet combustor. AIAA J 2018;56:4884–92. https://doi.org/10.2514/1.J057081.
[3] Mahto NK, Choubey G, Suneetha L, Pandey KM. Effect of variation of length-to-depth ratio and Mach number on the performance of a typical double cavity scramjet combustor. Acta Astronaut 2016;128:540–50. https://doi.org/10.1016/j.actaastro.2016.08.010.
[4] Huang Y, He X, Zhu Z, Zhu H. Inlet pressure effects on subatmospheric flame stabilization with an optimum size of a cavity-based combustor. Int J Aerosp Eng 2020;2020. https://doi.org/10.1155/2020/4126753.
[5] Sziroczak D, Smith H. A review of design issues specific to hypersonic flight vehicles. Prog Aerosp Sci 2016;84:1–28. https://doi.org/10.1016/j.paerosci.2016.04.001.
[6] Chen S, Zhao D. Numerical study of non-reacting flowfields of a swirling trapped vortex ramjet combustor. Aerosp Sci Technol 2018;74:81–92. https://doi.org/10.1016/j.ast.2018.01.006.
[7] Choubey G, Devarajan Y, Huang W, Mehar K, Tiwari M, Pandey KM. Recent advances in cavity-based scramjet engine- a brief review. Int J Hydrogen Energy 2019;44:13895–909. https://doi.org/10.1016/j.ijhydene.2019.04.003.
[8] Zuo FY, Mölder S. Hypersonic wavecatcher intakes and variable-geometry turbine based combined cycle engines. Prog Aerosp Sci 2019;106:108–44. https://doi.org/10.1016/j.paerosci.2019.03.001.
[9] Dong Z, Sun M, Wang Z, Chen J, Cai Z. Survey on key techniques of rocket-based combined-cycle engine in ejector mode. Acta Astronaut 2019;164:51–68. https://doi.org/10.1016/j.actaastro.2019.07.016.
[10] Sun MB, Da CX, Wang HB, Bychkov V. Flame flashback in a supersonic combustor fueled by ethylene with cavity flameholder. J Propuls Power 2015;31:976–80. https://doi.org/10.2514/1.B35580.
[11] Wang H, Wang Z, Sun M, Wu H. Combustion modes of hydrogen jet combustion in a cavity-based supersonic combustor. Int J Hydrogen Energy 2013;38:12078–89. https://doi.org/10.1016/j.ijhydene.2013.06.132.
[12] Zhao D, Gutmark E, de Goey P. A review of cavity-based trapped vortex, ultra-compact, high-g, inter-turbine combustors. Prog Energy Combust Sci 2018;66:42–82. https://doi.org/10.1016/j.pecs.2017.12.001.
[13] Tong Y, Liu X, Wang Z, Richter M, Klingmann J. Experimental and numerical study on bluff-body and swirl stabilized diffusion flames. Fuel 2018;217:352–64. https://doi.org/10.1016/j.fuel.2017.12.061.
[14] Miao J, Fan Y, Wu W, Zhao S. Effect of air-assistant on ignition and flame-holding characteristics in a cavity-strut based combustor. Appl Energy 2020;116307. https://doi.org/10.1016/j.apenergy.2020.116307.
[15] Cao C, Ye T, Zhao M. Large eddy simulation of hydrogen/air scramjet combustion using tabulated thermo-chemistry approach. Chin J Aeronaut 2015;28:1316–27. https://doi.org/10.1016/j.cja.2015.08.008.
[16] Yang Y, Wang Z, Sun M, Wang H. Numerical simulation on ignition transients of hydrogen flame in a supersonic combustor with dual-cavity. Int J Hydrogen Energy 2016;41:690–703. https://doi.org/10.1016/j.ijhydene.2015.11.115.
[17] Morales AJ, Lasky IM, Geikie MK, Engelmann CA, Ahmed KA. Mechanisms of flame extinction and lean blowout of bluff body stabilized flames. Combust Flame 2019;203:31–45. https://doi.org/10.1016/j.combustflame.2019.02.002.
[18] Jones WP, Marquis AJ, Wang F. Large eddy simulation of a premixed propane turbulent bluff body flame using the Eulerian stochastic field method. Fuel 2015;140:514–25. https://doi.org/10.1016/j.fuel.2014.06.050.
[19] Shouse DT. Trapped vortex combustion technology. 2013-12-05] Http Ff Soliton, Ae Gatech, Edu/People/Lsankar/MITE Work Pdf 2000.
[20] Meyer TR, Brown MS, Fonov S, Goss LP, Gord JR, Shouse DT, et al. Optical diagnostics and numerical characterization of a trapped-vortex combustor. 38th AIAA/ASME/SAE/ASEE Jt Propuls Conf Exhib 2002. doi: 10.2514/6.2002-3863.
[21] Cai Z, Wang T, Sun M. Review of cavity ignition in supersonic flows. Acta Astronaut 2019;165:268–86. https://doi.org/10.1016/j.actaastro.2019.09.016.
[22] Zhang RC, Bai NJ, Fan WJ, Yan WH, Hao F, Yin CM. Flow field and combustion characteristics of integrated combustion mode using cavity with low flow resistance for gas turbine engines. Energy 2018;165:979–96. https://doi.org/10.1016/j.energy.2018.09.121.
[23] Agarwal KK, Krishna S, Ravikrishna RV. Mixing enhancement in a compact trapped vortex combustor. Combust Sci Technol 2013;185:363–78. https://doi.org/10.1080/00102202.2012.721034.
[24] Jin Y, He X, Jiang B, Wu Z, Ding G, Zhu Z. Effect of cavity-injector/radial-strut relative position on performance of a trapped vortex combustor. Aerosp Sci Technol 2014;32:10–8. https://doi.org/10.1016/j.ast.2013.12.014.
[25] Li M, He X, Zhao Y, Jin Y, Ge Z, Sun Y. Dome structure effects on combustion performance of a trapped vortex combustor. Appl Energy 2017;208:72–82. https://doi.org/10.1016/j.apenergy.2017.10.029.
[26] Zhang RC, Hao F, Fan WJ. Combustion and stability characteristics of ultra-compact combustor using cavity for gas turbines. Appl Energy 2018;225:940–54. https://doi.org/10.1016/j.apenergy.2018.05.084.
[27] Jin Y, He X, Jiang B, Wu Z, Ding G. Design and performance of an improved trapped vortex combustor. Chin J Aeronaut 2012;25:864–70. https://doi.org/10.1016/S1000-9361(11)60456-1.
[28] Li M, He X, Zhao Y, Jin Y, Yao K, Ge Z. Performance enhancement of a trapped-vortex combustor for gas turbine engines using a novel hybrid-atomizer. Appl Energy 2018;216:286–95. https://doi.org/10.1016/j.apenergy.2018.02.111.
[29] Zhang RC, Bai NJ, Fan WJ, Huang XY, Fan XQ. Influence of flame stabilization and fuel injection modes on the flow and combustion characteristics of gas turbine combustor with cavity. Energy 2019;189. https://doi.org/10.1016/j.energy.2019.116216.
[30] Chen Y, Zhai W, Fan Y. Fuel distribution and evaporation characteristics downstream of an integrated flameholder. Fuel 2020;266:117009. https://doi.org/10.1016/j.fuel.2020.117009.
[31] Merlin C, Domingo P, Vervisch L. Large eddy simulation of turbulent flames in a trapped vortex combustor (TVC) – a flamelet presumed-pdf closure preserving laminar flame speed. Comptes Rendus – Mec 2012;340:917–32. https://doi.org/10.1016/j.crme.2012.10.039.
[32] Ezhil Kumar PK, Mishra DP. Numerical simulation of cavity flow structure in an axisymmetric trapped vortex combustor. Aerosp Sci Technol 2012;21:16–23. https://doi.org/10.1016/j.ast.2011.04.007.
[33] Zhang RC, Fan WJ, Shi Q, Tan WL. Combustion and emissions characteristics of dual-channel double-vortex combustion for gas turbine engines. Appl Energy 2014;130:314–25. https://doi.org/10.1016/j.apenergy.2014.05.059.
[34] Denman ZJ, Wheatley V, Smart MK, Veeraragavan A. Supersonic combustion of hydrocarbons in a shape-transitioning hypersonic engine. Proc Combust Inst 2017;36:2883–91. https://doi.org/10.1016/j.proci.2016.08.081.
[35] Choubey G, Pandey KM. Effect of variation of inlet boundary conditions on the combustion flow-field of a typical double cavity scramjet combustor. Int J Hydrogen Energy 2018;43:8139–51. https://doi.org/10.1016/j.ijhydene.2018.03.062.
[36] Roquemore WM, Shouse D, Burrus D, Johnson A, Cooper C, Duncan B, et al. Trapped vortex combustor concept for gas turbine engines. 39th Aerosp Sci Meet Exhib. 2001.
[37] Barnes FW, Segal C. Cavity-based flameholding for chemically-reacting supersonic flows. Prog Aerosp Sci 2015;76:24–41. https://doi.org/10.1016/j.paerosci.2015.04.002.
[38] Wu Z, Zhou X, Liu X, Ni Y, Zhao K, Peng F, et al. Investigation on the dependence of flash point of diesel on the reduced pressure at high altitudes. Fuel 2016;181:836–42. https://doi.org/10.1016/j.fuel.2016.05.062.
[39] Okai K, Himeno T, Watanabe T, Kobayashi H, Taguchi H. Investigation of combustion and altitude-ignition performance of a small hydrogen-fueled reversed-flow turbine combustor. 52nd Aerosp Sci Meet 2014:1–9. doi: 10.2514/6.2014-1541.
[40] Black DO, Messing WE. Effect of three flame-holder configurations on sub- sonic flight performance of rectangular ram jet over range of altitudes. NACA 1948.
[41] Drabble JS. Investigation into the Performance of a "REID" Forced Air Blast Ramjet Combustion Chamber on a Low Pressure Combustion Rig. NASA TN GW 1953.
[42] Read RW, Rogerson JW, Hochgreb S. Relight imaging at low temperature, low pressure conditions. In: 46th AIAA Aerosp Sci Meet Exhib; 2008. https://doi.org/10.2514/6.2008-957.
[43] Nguyen DN, Ishida H, Shioji M. Ignition and combustion characteristics of gas-to-liquid fuels for different ambient pressures. Energy Fuels 2010;24:365–74. https://doi.org/10.1021/ef9008532.

[44] Chen BH, Liu JZ, Yao F, He Y, Yang WJ. Ignition delay characteristics of RP-3 under ultra-low pressure (0.01–0.1 MPa). Combust Flame 2019;210:126–33. https://doi.org/10.1016/j.combustflame.2019.08.009.
[45] Zhang Y, He X, Zhu H. Study on atomization performance of multi-orifice air-assisted plain jet atomizers. Fuel 2021;286:119428. https://doi.org/10.1016/j.fuel.2020.119428.
[46] Liu J, Hu E, Zeng W, Zheng W. A new surrogate fuel for emulating the physical and chemical properties of RP-3 kerosene. Fuel 2020;259:116210. https://doi.org/10.1016/j.fuel.2019.116210.
[47] Jiang P, He X. Ignition characteristics of a novel mixed-flow trapped vortex combustor for turboshaft engine. Fuel 2020;261:116430. https://doi.org/10.1016/j.fuel.2019.116430.
[48] Lefebvre AH, Ballal DR. Gas turbine combustion. third ed. New York: Taylor & Francis Group; 2010.
[49] Holman JP. Experimental methods for engineers. Seventh ed. Mc Graw-Hill; 2007.